

UNesT: Local Spatial Representation Learning with Hierarchical Transformer for Efficient Medical Segmentation

Xin Yu¹, Qi Yang¹, Yinchu Zhou¹, Leon Y. Cai², Riqiang Gao^{1,3}, Ho Hin Lee¹, Thomas Li², Shunxing Bao⁴, Zhoubing Xu³, Thomas A. Lasko⁵, Richard G. Abramson^{2,6}, Zizhao Zhang⁷, Yuankai Huo^{1,4}, Bennett A. Landman^{1,2,4,5}, Yucheng Tang^{4,8}

¹*Department of Computer Science, Vanderbilt University, Nashville, TN, USA 37212*

²*Department of Biomedical Engineering, Vanderbilt University, Nashville, TN, USA, 37212*

³*Digital Technology and Innovation, Siemens Healthineers, Princeton, NJ, USA, 08540*

⁴*Department of Electrical and Computer Engineering, Vanderbilt University, Nashville, TN, USA, 37212*

⁵*Department of Biomedical Informatics, Vanderbilt University Medical Center, Nashville, TN, USA, 37235*

⁶*Annalise-AI, Pty, Ltd*

⁷*Google Cloud AI*

⁸*Nvidia Corporation*

Abstract

Transformer-based models, capable of learning better global dependencies, have recently demonstrated exceptional representation learning capabilities in computer vision and medical image analysis. Transformer reformats the image into separate patches and realizes global communication via the self-attention mechanism. However, positional information between patches is hard to preserve in such 1D sequences, and loss of it can lead to sub-optimal performance when dealing with large amounts of heterogeneous tissues of various sizes in 3D medical image segmentation. Additionally, current methods are not robust and efficient for heavy-duty medical segmentation tasks such as predicting a large number of tissue classes or modeling globally inter-connected tissues structures. To address such challenges and inspired by the nested hierarchical structures in vision transformer, we proposed a novel 3D medical image segmentation method (UNesT), employing a simplified and faster-converging transformer encoder design that achieves local communication among spatially adjacent patch sequences by aggregating them hierarchically. We extensively validate our method on multiple challenging datasets, consisting of multiple modalities, anatomies, and a wide range of tissue classes including 133 structures in the brain, 14 organs in the abdomen, 4 hierarchical components in the kidneys, and inter-connected kidney tumors. We show that UNesT consistently achieves state-of-the-art performance and evaluate its generalizability and data efficiency. Particularly, the model achieves whole brain segmentation task complete ROI with 133 tissue classes in a single network, outperforms prior state-of-the-art method SLANT27 ensembled with 27 networks, our model performance increases the mean DSC score of the publicly available Colin and CANDI dataset from 0.7264 to 0.7444 and from 0.6968 to 0.7025, respectively. Code, pre-trained models, and use case pipeline are integrated with the open-source framework MONAI available at: <https://github.com/Project-MONAI/model-zoo/tree/dev/models>.

Keywords: Hierarchical Transformer, Whole Brain Segmentation, Renal Substructure Segmentation

1. Introduction

Medical image segmentation tasks have become increasingly challenging due to the need for modeling hundreds of tissues (Huo et al., 2019; Wasserthal et al., 2022) or hierarchically inter-connected structures (Landman et al., 2015) in 3D volumes. In the past few years, convolutional neural networks (CNNs) have dominated medical image segmentation due to their superior performance. Among all the CNNs, the U-Net (Ronneberger et al., 2015) and its variants have been the most widely used for medical image segmentation. A "U-shape" model generally consists of an encoder for global representation learning and a decoder to gradually decode the learned representation to a pixel-wise segmentation. However, CNNs-

based models' encoding performance is limited because of their localized receptive fields (Hu et al., 2019).

Vision Transformers (ViT), on the other hand, are capable of learning long-range dependencies and have recently demonstrated exceptional representational learning capabilities and effectiveness in computer vision and medical image applications (Dosovitskiy et al., 2020; Hatamizadeh et al., 2022; Zhou et al., 2021a). Unlike CNNs, ViTs learn better long-range information by tokenizing images into 1D sequences and leveraging the self-attention blocks to facilitate global communication (Hatamizadeh et al., 2022), which makes transformers better encoders. However, by tokenizing the image into 1D patches, transformers are less able to capture local positional information compared to CNNs, due to the lack of locality inductive bias

inherent to CNNs (Cordonnier et al., 2019; Dosovitskiy et al., 2020). To overcome this, ViT usually requires a large amount of training data which is expensive to acquire (Tang et al., 2022; Zhou et al., 2021a). With small datasets in the medical field, insufficient data can lead to model inefficiency, especially when dealing with a large number of tissues of various sizes. Moreover, the self-attention mechanism for modeling multi-scale features for high-resolution medical volumes is computationally expensive (Beltagy et al., 2020; Han et al., 2021; Liu et al., 2021).

To improve representation learning in transformers in small datasets, recent works envision the use of local self-attention (Liu et al., 2021; Cao et al., 2021; Han et al., 2021). To leverage information across embedded sequences, "shifted window" transformers (Liu et al., 2021) have been proposed for dense predictions and modeling multi-scale features. However, these attempts aiming to adapt the self-attention mechanism by modifying patch communication often yield high computational complexity. In addition, the Swin transformer under-performs when datasets are small or there are a large number of structures (Liu et al., 2021).

Considering the advantages of hierarchical models (Ç. et al., 2016; Roth et al., 2018; Tang et al., 2022) on modeling heterogeneous high-resolution radiographic images and inspired by the aggregation function in the nested ViT (Zhang et al., 2021c), we propose a Hierarchical hybrid 3D U-shape medical segmentation model with Nested Transformers (UNesT). Specifically, with nested transformers as the encoder, UNesT hierarchically encodes features with the 3D block aggregation function and merges with the convolutional-based decoder via skip connections at various resolutions to enable learning of local behaviors for small structures or small datasets. The 3D nested structure retains the original global self-attention mechanism and achieves information communication across patches by stacking transformer encoders hierarchically.

We perform extensive experiments to validate the performance of UNesT on the challenging whole brain segmentation task with 133 classes using T1 weighted (T1w) MRI images and a collected renal substructures 3D CT volumetric dataset with 116 patients on characterizing multiple kidney components including renal cortex, medulla and pelvicalyceal system with kidney function. We further evaluate UNesT on two widely-used public datasets Beyond The Cranial Vault (BTCV) (Landman et al., 2015) and KiTS19 (Heller et al., 2021) to illustrate the generalizability of UNesT. We compare UNesT to recent convolutional and transformer-based 3D medical segmentations baselines and conduct scalability and data efficiency analysis in a low-data regime. Baselines are built with the same framework for a fair comparison.

Our contributions in this work can be summarized as:

- We introduce a novel 3D hierarchical block aggregation module, and propose a new transformer-based 3D medical segmentation model, dubbed UNesT. The model provides local spatial patch communication, to better capture various tissues. This method achieves hierarchical modeling of high-resolution medical images and outperforms local self-attention variants with a simplified design compared to

the "shifted window" module leading to improved data efficiency.

- We validate UNesT on a whole brain segmentation task that contains hundreds of classes. UNesT outperforms the current convolutional- and transformer-based single model methods. Our single model also outperforms prior top method SLANT27 (Huo et al., 2019), which ensembles 27 networks, and achieves new state-of-the-art performance.
- We collect and manually delineate the first in-house renal substructure dataset (116 CT subjects). We show that our method achieves state-of-the-art performance for accurately measuring cortical, medullary, and pelvicalyceal system volumes. We demonstrate the clinical utility of this work through accurate volumetric analysis, strong correlations, and robust reproducibility. We also introduce MONAI Bundle, a new plug-and-use framework for deploying models, our codes, trained models, and tutorials are released for public availability.
- We investigate model scalability and data efficiency in low-data regimes as well as the impact of the size of pre-training dataset. We show the proposed method's generalizability by validating it on public datasets: BTCV and KiTS19.

2. Related Works

Medical Segmentation with Transformers. Transformer models demonstrate the ability of modeling longer-range dependencies for high dimension and high-resolution medical images in 3D Space. The scalability, generalizability, and efficiencies of ViT and hierarchical transformers enable stronger representation learning for dense predictions (e.g., pixel-to-pixel segmentation). Medical image segmentation tasks are embedding learning problems with multi-scale features instead of fixed scale such as word tokens. To employ the vanilla Transformer (Dosovitskiy et al., 2020) for medical images, recent works proposed variant architectures that use ViT as network components. There are four typical configurations for transformer-based medical image segmentation models.

The major adoption of transformers in the segmentation model is to use successive blocks as the encoder (Hatamizadeh et al., 2022; Peiris et al., 2021; Tang et al., 2022). The advantage of sequence-to-sequence modeling as the first embedding for medical images is to directly generate tokenized patches for the feature representation. Most of these methods connect a convolutional neural network (CNN)-based decoder and form the "U-shape" architecture for segmentation. This design features the long-range modeling ability for input images with transformer encoder and better inductive bias with CNN decoder.

Due to the lack of inductive bias in transformer models, researchers propose to encode image features with CNN networks as the main encoder, adopting the advantages of global feature modeling. One early use of vanilla transformer blocks for medical segmentation is the TransUNet (Chen et al., 2021b), which used 12 2D transformer layers for encoding bottleneck features. TransUNet++ (Wang et al., 2022), AFter-UNet (Yan et al., 2022), TransClaw (Chang et al., 2021), Ds-TransUNet (Lin

et al., 2021), TransAttUNet (Chen et al., 2021a) and GT-UNet (Li et al., 2021b) improved the self-attention blocks, and achieved promising performance in CT segmentation. In addition, TransBTS (Wang et al., 2021c), CoTr (Xie et al., 2021a) and TransBridge (Deng et al., 2021) explored variant modules such as deformable transformer blocks for 3D image segmentation tasks. Later, SegTrans (Li et al., 2021a), MT-UNet (Wang et al., 2021a) introduced squeeze and expansion mechanism and mixed structure for modeling context affinities. BAT (Wang et al., 2021b) and Poly-PVT (Dong et al., 2021) used grouping or boundary-aware designs to improve transformer robustness with cross-slice attention.

Another architecture type adopting transformers is fusion models. The multiple branch design of encoders has CNN and transformer in parallel. The encoded representations by two encoders are then fused into a single decoder. TransFuse (Zhang et al., 2021a), FusionNet (Meng et al., 2021) are pioneering works that benefit from learning global and local features. The PMtrans (Zhang et al., 2021b) and X-Net (Li et al., 2021c) introduce a multi-branch pyramid and a dual encoding network which demonstrate leading results on pathology images. MedT (Valanarasu et al., 2021) and Ds-TransUNet (Lin et al., 2021) proposed a CNN global branch and a local transformer branch with an axial self-attention module. With a fusion model, input medical images are split into both whole feature and non-overlapping patches followed by two encoder branches. With fusion designs, model complexities are commonly large due to the additional encoding branches, which is a disadvantage of these models.

Recently, scientists have investigated the full adoption of transformer models for medical image segmentation. There are challenges in using pure transformer models, especially for 3D images due to the limitation of inductive bias and the high complexity of transformers. Swin UNet (Cao et al., 2021) is a pure transformer model designed for 2D medical images. It adopted the "U-shape" architecture and used a skip connection that connect the encoded features to the transformer decoder. D-Former (Wu et al., 2022) utilized dynamic position encoding blocks and local scope modules for improving local feature representation learning. MISSformer (Huang et al., 2021) is a pure transformer network with feed-forward enhanced blocks in its transformer modules. This design leveraged long-range dependencies with local features at different scales. The nnFormer (Zhou et al., 2021a) is another promising network that used 3D transformers and combined encoder and decoder with self-attention operations. nnFormer incorporated a skip attention mechanism to replace simple skip-connections, which outperformed CNN-based methods significantly. Though the use of pure transformers as the model is more intuitive and better for design consistency; Yet, there are still uncharted areas using self-attention in the decoder. High model complexity can cause unsatisfied robustness and is challenging to explore in 3D context.

Pre-training transformers with a large-scale dataset is of potential value to boost transformer model performance (Dosovitskiy et al., 2020). Empirical studies (Zhai et al., 2021) show that the transformer model can have better scalability when more data are fed. In the medical domain, researchers have explored

self-supervised pre-training approaches with CNNs (Zhou et al., 2021b). More recently, pre-training 3D transformers (Tang et al., 2022) for radiological images have been presented. Furthermore, uniformed pre-training frameworks (Xie et al., 2021c,b) are shown to construct teacher-student models for medical data. However, the use of pre-training is computationally exhaustive. In this paper, we aim to simplify and evaluate the effect of the pre-training framework with empirical studies.

Hierarchical Feature Aggregation. The aggregation of multi-level features could improve segmentation results by merging the features extracted from different layers. Modeling hierarchical features, such as U-Net (Ç. et al., 2016) and pyramid networks (Roth et al., 2018), multi-scale representations are leveraged. The extended feature pyramids compound the spatial and semantic information through two structures, iterative deep layer aggregation which fuses multi-scale information as well as hierarchical deep aggregation which fuses representations across channels. In addition to single network, nested UNets (Zhou et al., 2018), nnUNets (Isensee et al., 2021), coarse-to-fine (Zhu et al., 2018) and Random Patch (Tang et al., 2021a) suggest multi-stage pathways enrich the different semantic levels of features progressively with cascaded networks. Different from the above CNN-based methods, we explore the use of data-efficient transformers for modeling hierarchical 3D features by block aggregation.

3. Method

3.1. Hierarchical Transformer Encoder

The overall UNesT architecture is shown in Fig. 1. The input image is a sub-volume $\mathcal{X} \in \mathbb{R}^{H \times W \times D \times C}$ and the volumetric embedding token has a patch size of $S_h \times S_w \times S_d \times C$. 3D tokens are projected onto a size of $\frac{H}{S_h} \times \frac{W}{S_w} \times \frac{D}{S_d} \times C'$ in the patch projection step, where C' is the embedded dimension. Following the motivation in (Zhang et al., 2021c) for efficient non-local communication, all projected sequences of embeddings are partitioned to blocks (blockify) with a resolution of $\mathcal{X} \in \mathbb{R}^{b \times T \times n \times C'}$, where T is the number of blocks at the current hierarchy, b is the batch size, n is the total length of sequences. Detailed illustration of the blockify mechanism is shown in Fig. 1. The dimensions of the embeddings follow $T \times n = \frac{H}{S_h} \times \frac{W}{S_w} \times \frac{D}{S_d}$. Each block is fed into sequential transformer layers separately, which consist of the canonical multi-head self-attention (MSA), multi-layer perceptron (MLP), and layer normalization (LN). We add learnable position embeddings to sequences for capturing spatial relations before the blocked transformers. The output of encoder layers $t-1$ and t are computed as follows:

$$\begin{aligned}\hat{z}^t &= \text{MSA}_{\text{HRCY}_l}(\text{LN}(z^{t-1})) + z^{t-1}, t = 1 \dots L \\ z^t &= \text{MLP}(\text{LN}(\hat{z}^t)) + \hat{z}^t, t = 1 \dots L\end{aligned}\quad (1)$$

where $\text{MSA}_{\text{HRCY}_l}$ denotes the multi-head self-attention layer of hierarchy l , \hat{z}^t and z^t are the output representations of MSA and MLP and L denotes the number of transformer layers. In practice, $\text{MSA}_{\text{HRCY}_l}$ is applied in parallel to all partitioned blocks:

$$\begin{aligned}\text{MSA}_{\text{HRCY}_l}(\mathbf{Q}, \mathbf{K}, \mathbf{V}) &= \text{Stack}(\text{BLK}_1, \dots, \text{BLK}_T) \\ \text{BLK} &= \text{Attention}(\mathbf{Q}, \mathbf{K}, \mathbf{V}) = \text{Softmax}\left(\frac{\mathbf{Q}\mathbf{K}^T}{\sqrt{d}}\right)\mathbf{V},\end{aligned}\quad (2)$$

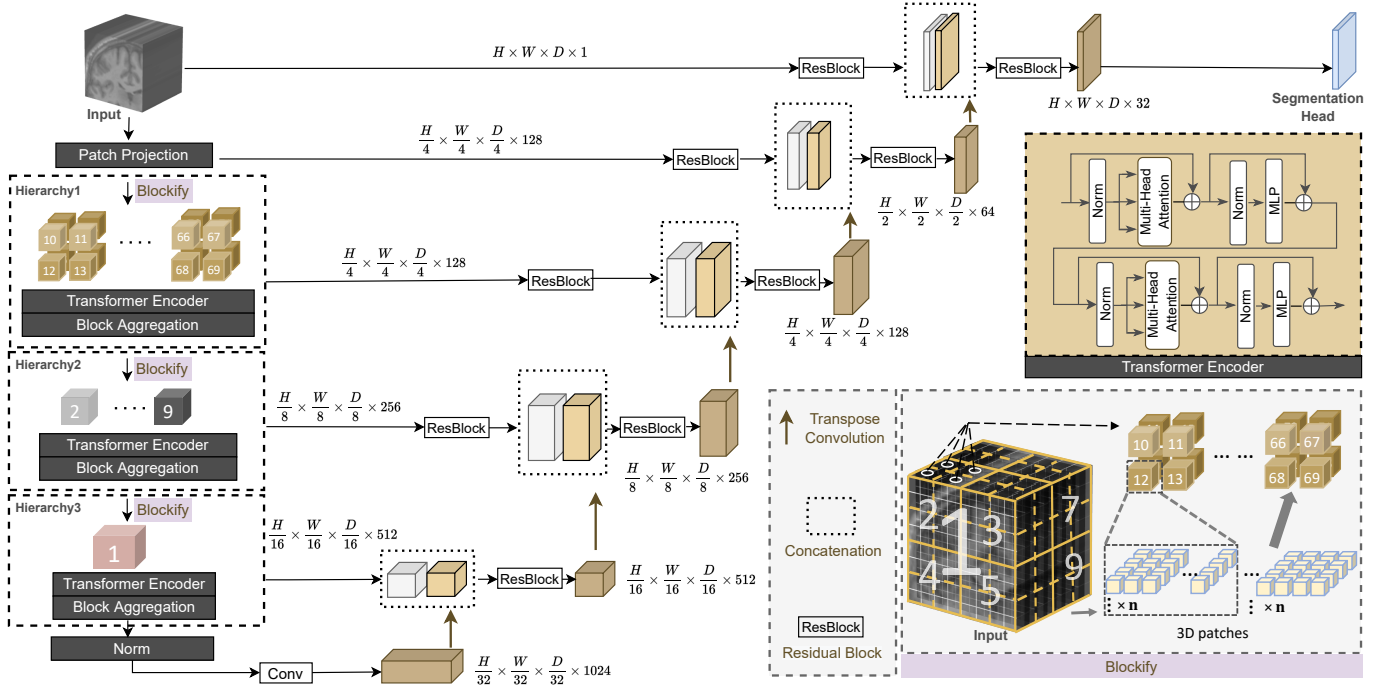


Figure 1: Overview of the proposed UNeST with the hierarchical transformer encoder. Input image volumes are embedded into patches. In each hierarchy, patch embeddings are blockified and fed into the transformer encoder. Block aggregation and image feature down-sampling are performed between hierarchies.

where Q, K, V denotes queries, keys, and value vectors in the multi-head attention, and σ is the size of each vector. All blocks at each level of the hierarchy share the same parameters given the input X , which leads to hierarchical representations without increasing complexity.

3.2. 3D Block Aggregation

We extend the spatial nesting operations in (Zhang et al., 2021c) to 3D blocks where each volume block is modeled independently. Information across blocks is communicated by the aggregation module. The feature map starts with size of $\frac{H}{S_h} \times \frac{W}{S_w} \times \frac{D}{S_d} \times C'$ at the first hierarchy and downsamples by factor of 2 for each dimension at the start of the following hierarchy. The feature maps then are blockified to aforementioned size of $T \times n \times C'$. Since the feature size is reduced by $2 \times 2 \times 2$, and the sequence length n remains the same, the number of blocks T reduce by a factor of 8 in each hierarchy as a result. After feeding through the transformer layer, blocks are unblocked to the input feature size with the block aggregation operation. There are three hierarchies in our model design which results in a total number of 64, 8, and 1 blocks in each hierarchy. In the volumetric plane, the encoded blocks are merged among adjacent block representations. The design and use of the aggregation modules in the 3D scenario leverage local attention.

3.3. Decoder

To better capture localized information and further reduce the effects of lacking inductive bias in transformers, we use a hybrid design with a convolution-based decoder for segmentation.

We use a patch size of $4 \times 4 \times 4$ in our encoder. The patch embedded dimension is set to 128 so that the feature size is $\frac{H}{4} \times \frac{W}{4} \times \frac{D}{4} \times 128$ after patch projection. The 3 hierarchies have

a number of transformer layers (depth) of 2, 2, and 8 and embedded dimensions (width) of 128, 256, and 512, respectively. The feature size at the end of each hierarchy are $\frac{H}{4 \times 2^i} \times \frac{W}{4 \times 2^i} \times \frac{D}{4 \times 2^i} \times C$ where $i = 0, 1, 2$ and $C = 128, 256, 512$, as shown in Fig. 1. The feature map from the last hierarchy is fed into a layer normalization layer to generate the transformer encoder output. Since the feature size from each hierarchy have multiple resolutions and are inspired by the U-shape models (Ronneberger et al., 2015), we merge the multi-resolution features with the decoder with skip connections followed by convolutional layers.

The bottleneck is generated by feeding the output of the encoder to a $3 \times 3 \times 3$ convolutional layer. We upsample the bottleneck by applying a transpose convolutional layer. The output of the transposed convolution is concatenated with the prior hierarchical representations and fed into a residual block consisting of two $3 \times 3 \times 3$ convolutional layers followed by instance normalization (Ulyanov et al., 2016) layers. The features from the residual block of each hierarchy or patch projection level are then upsampled by transposing convolutional layers and concatenated with the upper hierarchy, patch or image representation processed by the aforementioned residual block. The segmentation mask is acquired by $1 \times 1 \times 1$ convolutional layer with a softmax activation function. Compared to some prior related works such as TransBTS (Wang et al., 2021c) and CoTr (Xie et al., 2021a), our design employs the hierarchical transformer directly on images and extract representations at multiple scales without convolutional layers.

4. Experiments

4.1. Dataset

Whole Brain Segmentation Dataset. Training and testing data are MRI T1-weighted (T1w) 3D volumes from 10 different sites. Training set consists of 50 scans from the Open Access Series on Imaging Studies (OASIS) (Marcus et al., 2007) dataset which is manually traced to 133 labels based on the BrainCOLOR protocol (Klein et al., 2010) by Neuromorphometrics Inc. The size of the data are $256 \times 256 \times [270, 334]$ with 1 mm isotropic spacing. The testing cohort contains Colin27 (Colin) T1w scan (Aubert-Broche et al., 2006) and 13 T1w MRI scans from the Child and Adolescent Neuro Development Initiative (CANDI) (Kennedy et al., 2012) dataset. The Colin dataset contains one high-resolution scan averaging from 27 scans of the same subject. The label is manually traced to 130 labels based on BrainCOLOR protocol. The size of the scan is $362 \times 362 \times 434$ with 0.5mm isotropic spacing. The CANDI dataset is manually traced to 130 labels following the BrainCOLOR protocol. The size of the scans are $256 \times 256 \times 128$ with spacing of $0.94\text{mm} \times 0.94\text{mm} \times 1.5\text{mm}$. A detailed class name and the 3 classes not labeled in the test sets can be found in Table A.8 in the supplementary material. The CANDI dataset contains a different age group (5-15 years old) compared to the OASIS training cohort (18-96 years old), which allowed assessment to the different populations. Following the same practice in (Huo et al., 2019), we use auxiliary labels comprising of 4859 T1w MRI scans from eight different sites whose labels are generated by using an existing multi-atlas segmentation pipeline (Asman and Landman, 2014) to pre-train the model and finetune the pre-trained model with the 50 manually traced data from the OASIS dataset. A detailed summary of the 4859 multi-site images is shown in Table 1.

Renal Substructure Dataset. We construct an internal cohort of the renal substructures segmentation dataset with 116 subjects imaged under institutional review board (IRB) approval (IRB #131461). Cortex, medulla, and pelvicalyceal systems are labeled in the dataset (Fig. 2). Data with ICD codes related to kidney dysfunction are excluded since they could potentially influence kidney anatomy. The left and right renal structures are outlined manually by three interpreters under the supervision of clinical experts. The renal columns are included in the cortex label. The medulla is surrounded by the cortex, and the pelvicalyceal systems contain calyces and pelvis that drain into the ureter. All manual labels are verified and corrected independently by expert observers. For the test set of 20 subjects, we perform a second round of manual segmentation (interpreter 2) to assess the intra-rater variability and reproducibility. The image size of each scan is $512 \times 512 \times [90, 131]$ with spacing of $[0.54, 0.98]\text{mm} \times [0.54, 0.98]\text{mm} \times 3.0\text{mm}$.

Multi-organ Segmentation (BTCV) Dataset. We evaluate model generalizability with the Beyond The Cranial Vault (BTCV) dataset. It is comprised of 100 de-identified contrast-enhanced CT volumes with 13 labeled anatomies, including spleen, right kidney, left kidney, gallbladder, esophagus, liver, stomach, inferior vena cava (IVC), portal and splenic veins (PSV), pancreas, right and left adrenal gland. The image size of each scan is $512 \times 512 \times [80, 255]$ with the spacing of

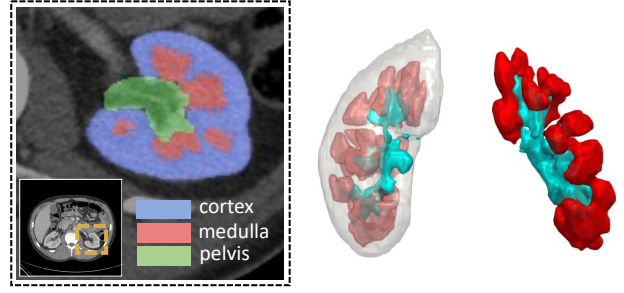


Figure 2: Visual and 3D illustration of the kidney components.

$[0.54, 0.98]\text{mm} \times [0.54, 0.98]\text{mm} \times [2.5, 7.0]\text{mm}$. 50 scans are publicly available in the MICCAI 2015 Multi-atlas Labeling Challenge (Landman et al., 2015), in which 20 scans are used for public testing.

KiTS19. To further validate the generalizability of the proposed method for characterizing renal tissues, we apply the model to the public KiTS19 dataset. The KiTS19 (Heller et al., 2021) task focuses on the whole kidney and kidney tumor segmentation. Images and labels from 210 subjects are publicly available. The image size of each scan is $512 \times [512, 796] \times [29, 1059]$ with spacing of $[0.44, 1.04]\text{mm} \times [0.44, 1.04]\text{mm} \times [0.5, 5.0]\text{mm}$.

4.2. Implementation Details

For a fair comparison, all the transformer-based baseline models are integrated in the same framework to make sure the comparison is focused on the model architecture rather than hyperparameter tuning. Experiments are implemented in Pytorch and MONAI¹. All segmentation models are trained with a single Nvidia RTX 5000 16G GPU with an input volume size of $96 \times 96 \times 96$. Models are optimized with a warm-up cosine scheduler of 500 steps.

4.2.1. Whole Brain Segmentation

During pre-training with auxiliary labels, the learning rate is initialized to 0.0001 with weight decay of $1e^{-5}$ to train for 200K iteration. During finetuning, the learning rate is set to $1e^{-5}$ to train for 50K iterations. As shown in Fig. 3, all data are registered to the MNI space using the MNI305 (Evans et al., 1993) template and preprocessed following the method in (Huo et al., 2019). All processed images have size of $172 \times 220 \times 156$ with isotropic spacing of 1mm. Registered input images are randomly cropped to the size of $96 \times 96 \times 96$ during the online augmentation. We use a five-fold cross-validation strategy during finetuning. The best performing model in each fold is selected to test on the external testing set and ensembled to get the final prediction in the MNI space. Predictions in MNI space are inverse transformed to the original space using NiftyReg (Ourselin et al., 2001) for evaluation (Fig. 3). Segmentation performances are evaluated using Dice similarity coefficient (DSC) and symmetric Hausdorff Distance (HD).

¹<https://monai.io/>

Table 1: Data summary of the 4859 multi-site images.

Study Name	Website	Images
Baltimore Longitudinal Study of Aging (BLSA)	www.blsa.nih.gov	614
Cutting Pediatrics	vkmc.mc.vanderbilt.edu/ebri	586
Autism Brain Imaging Data Exchange (ABIDE)	fcon_1000.projects.nitrc.org/indi/abide	563
Information Extraction from Images (IXI)	www.nitrc.org/projects/ixi_dataset	541
Attention Deficit Hyperactivity Disorder (ADHD200)	fcon_1000.projects.nitrc.org/indi/adhd200	950
Open Access Series on Imaging Study (OASIS)	www.oasis-brains.org	312
1000 Functional Connectome (fcon_1000)	fcon_1000.projects.nitrc.org	1102
Nathan Kline Institute Rockland (NKI_rockland)	fcon_1000.projects.nitrc.org/indi/enhanced	141

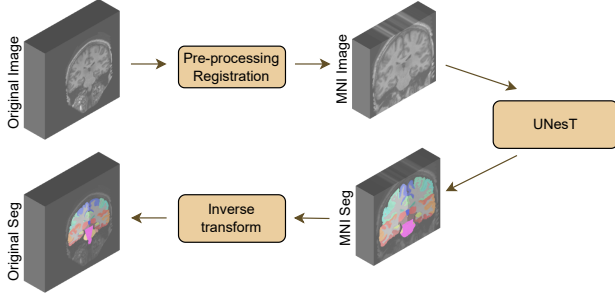


Figure 3: Overview of the workflow for the whole brain segmentation task. Original images are pre-processed and registered to the MNI space before feeding into the networks. Model outputs that are in MNI space are transformed back to the original space to get the final predictions.

4.2.2. Renal Substructures Segmentation

Five-fold cross-validation is used for all experiments on 96 subjects, while 20 subjects are used for held-out testing. The five-fold models’ ensemble is used for inference and evaluating test set performance. For experiment training, we used 1) a CT window range of $[-175, 275]$ HU; 2) scaled intensities of $[0.0, 1.0]$ with 1.0mm isotropic spacing. The learning rate is initialized to 0.0001 followed by a decay of $1e^{-4}$ for 50K iterations. For fair comparison and direct evaluation of the effectiveness of models, no pre-training is performed for all segmentation tasks. Segmentation results are evaluated with DSC and HD. We conduct volumetric analyses on kidney components in terms of R squared error, Pearson R, absolute deviation of volume, and the percentage difference between the proposed method and manual label.

4.2.3. Multi-organ Segmentation

80 subjects are used for training/validation and 20 are used for testing. The images are resampled to $1.5\text{mm} \times 1.5\text{mm} \times 2.0\text{mm}$. Common data augmentation such as random flip, rotation, and change of intensity are applied with the probability of 0.1. The learning rate is initialized to 0.0001 followed by a decay of $1e^{-4}$ for 100K iterations. Segmentation results are evaluated with DSC.

4.2.4. Kidney and Kidney Tumor Segmentation

We perform five-fold cross-validation experiments on 210 subjects and show DSC results of the held-out 20%. The experiments have the same settings as the renal substructures dataset.

5. Results

We evaluate the UNesT performance against recent convolutional- (Isensee et al., 2021) and transformer-based (Wang et al., 2021c; Zhou et al., 2021a; Hatamizadeh et al., 2022; Tang et al., 2022) 3D medical segmentation baselines. UNesT presents distinguished results on the task of whole brain segmentation with 133 tissue classes. Next, we perform experiments on the first kidney substructures CT dataset. We further validate model generalizability with the publicly available BTCV and KiTS19 datasets.

5.1. Whole Brain Segmentation

A detailed comparison of quantitative performance is shown in Table 2 and Fig. 4. The qualitative performance is shown in Fig. 5. All the models are pre-trained with 4859 auxiliary pseudo labels and are finetuned with 50 manually traced labels from OASIS in the 5-fold ensemble setting. We first compare the proposed UNesT model with nnUNet (Isensee et al., 2021) and several transformer-based methods. Most of the methods have infinite HD on the CANDI dataset associated with 0.43 to 0.64 DSC score indicating those methods fail to predict all of the 130 classes in the external testing set. UNETR performs the best among these widely used 3D medical image segmentation methods. Compared with UNETR, UNesT improves the performance in the Colin (from 0.7320 to 0.7444) and the CANDI (from 0.6851 to 0.7025) dataset by a margin. SLANT27 (Huo et al., 2019), the prior state-of-the-art method, divides the whole brain into 27 parts and ensembles 27 tiled 3D-UNet (Ç. et al., 2016) for the final predictions. Within the same 5-fold ensemble settings, UNesT ensemble with 5 models outperforms SLANT27 ensemble with 135 models in terms of DSC in both Colin (0.7444 vs. 0.7264) and CANDI (0.7025 vs. 0.6968) dataset and achieves the state-of-the-art performance. UNesT achieves significant improvement on the test set compared to SLANT27 with $p < 0.05$ under Wilcoxon signed-rank test and further reduces the variation of DSC score distribution with tighter quartiles (Fig. 4). In Fig. 5, we show UNesT has better captures on the boundary and correctly segments brain tissues. As the external testing set represents a high resolution and different age population cohort, we show that our method can generalize learned knowledge to different populations.

5.2. Characterization of Renal substructures

Segmentation Results. Compared to canonical kidney studies using shape models or random forests in Table 3, deep learning-

Table 2: Performance comparison for the whole brain segmentation task. Overall UNesT achieved state-of-the-art performance on the whole brain segmentation task. The number of parameters and GFLOPs (with a single input volume of $96 \times 96 \times 96$ for the transformer-based models) are shown. "×27" in SLANT27 represents that 27 of the same models are used. inf denotes part of data in the testing datasets have infinite HD. Notes: the FLOPs for SLANT27 are calculated based on input size of $96 \times 128 \times 88$ as designed in the paper (Huo et al., 2019).

Method	#Param	FLOPs(G)	Colin		CANDI	
			DSC	HD	DSC	HD
nnUNet (Isensee et al., 2021)	30.7M	358.6	0.7168	10.7321	0.4337	inf
TransBTS (Wang et al., 2021c)	33.0M	111.9	0.6537	inf	0.6043	inf
nnFormer (Zhou et al., 2021a)	158.9M	920.1	0.7113	10.2755	0.6393	inf
UNETR (Hatamizadeh et al., 2022)	92.6M	268.0	0.7320	10.3834	0.6851	11.1972
SwinUNETR (Tang et al., 2022)	62.2M	334.9	0.6854	22.0389	0.6537	34.3980
SLANT27 (Huo et al., 2019)	19.9M × 27	2051.0 × 27	0.7264	9.9061	0.6968	8.8851
UNesT	87.3M	261.7	0.7444	11.0081	0.7025	8.8417

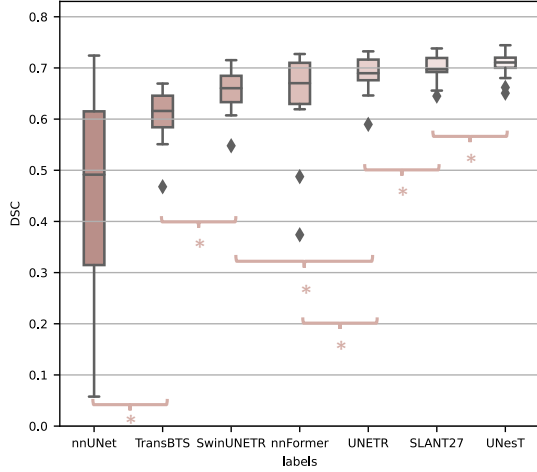


Figure 4: Quantitative results of the whole brain segmentation on the testing data. SLANT27 shows the smallest variation among the other baselines. UNesT achieves the overall best performance. Compared with SLANT27, UNesT further reduces the variation with improved median and quartiles of the DSC. * indicates statistically significant ($p < 0.05$) by Wilcoxon signed-rank test. Detailed quantitative performance comparison of 130 classes is shown in FigA.17 in the supplementary material.

based methods improve the performance by a large margin from 0.7233 to 0.7991. Among the nnUNet (Isensee et al., 2021) and extensive transformer models, we obtain the state-of-the-art average DSC score of 0.8564 compared to the second-best performance of 0.8411 from SwinUNETR, with a significant improvement $p < 0.05$ under Wilcoxon signed-rank test. We observe higher improvement on smaller anatomies such as the medulla and collecting systems. We compare qualitative results in Fig. 6. Our method demonstrates the distinct improvement of detailed structures for the medulla and pelvicalyceal systems. Fig. 7 shows that the proposed automatic segmentation method achieves better agreement compared to inter-rater assessment, 0.03 against 0.29 of mean difference indicating reliable reproducibility.

5.3. Multi-organ Segmentation

We present the quantitative performance and qualitative segmentation comparison on the BTCV dataset in Table 5 and Fig. 8, respectively. No pre-training or ensemble is performed

in all experiments. UNesT achieves the best average performance on BTCV dataset which demonstrate the generalizability of UNesT. Compared with the other methods, UNesT achieves large improvement on organs that are small in size such as the IVC, pancreas, and adrenal glands where UNesT outperforms the second best performing method by 1.5%, 1.2% and 2.1%, respectively. In Fig. 8 rows 1 and 2, UNesT successfully differentiates stomach tissues and background tissues demonstrating that UNesT has a better capability on identifying heterogeneous organs. UNesT better captures spatial information in Fig. 8 row 3, where most of the other model confuses right/left kidneys and liver/spleen tissues.

Volumetric Analysis. Table 4 lists the volume measurement with the proposed method. The UNesT achieves an R squared error of 0.9348 on the cortex. The correlation performance metric with Pearson R achieves 0.9896 for the UNesT against the manual label on the cortex. Our method obtains 2.5259 with an absolute deviation of volumes. The percent difference in the cortex is 3.8411. We observe the same trend for the Medulla and Pelvicalyceal System. Quantitative results show that our workflow can serve as the state-of-the-art volumetric measurement compared to the prior kidney characterization state-of-the-art (Tang et al., 2021b).

5.4. Kidney and Tumor Segmentation

To validate the generalizability of UNesT, we compare KiTS19 results among nnUNet (Isensee et al., 2021) and transformer-based methods. Our approach achieves moderate improvement at DSC of 0.9794 and 0.8439 for kidneys and tumors, respectively, as shown in Table 6, indicating that the designed architecture can be used as a generic 3D segmentation method. We show a qualitative comparison between our transformer-based model with the CNN-based nnUNet in Fig. 9. Case 1 is an above average sample that shows UNesT achieves a clearer boundary between kidney and tumor, while case 2 is an under average case where the 3D DSC score of UNesT achieves 0.80 compared to 0.72.

5.5. Ablation Study

5.5.1. Model Scales

To investigate the scalability of our proposed model, we designed "small", "base" and "large" UNesT models (UNesT-S,

Table 3: Segmentation results of the renal substructure on testing cases. The UNesT achieves state-of-the-art performance compared to prior kidney component studies and 3D medical segmentation baselines. * indicates statistically significant ($p < 0.05$) compared with the underlined performance by Wilcoxon signed-rank test.

Method	Cortex		Medulla		Pelvicalyceal System		Avg.	
	DSC	HD	DSC	HD	DSC	HD	DSC	HD
Chen et al. (Chen et al., 2012)	0.7512	40.1947	N/A	N/A	N/A	N/A	N/A	N/A
Xiang et al. (Xiang et al., 2017)	0.8196	27.1455	N/A	N/A	N/A	N/A	N/A	N/A
Jin et al. (Jin et al., 2016)	0.8041	34.5170	0.7186	32.1059	0.6473	39.9125	0.7233	35.5118
Tang et al. (Tang et al., 2021b)	0.8601	19.7508	0.7884	18.6030	0.7490	34.1723	0.7991	24.1754
nnUNet (Isensee et al., 2021)	0.8915	17.3764	0.8002	18.3132	0.7309	31.3501	0.8075	22.3466
TransBTS (Wang et al., 2021c)	0.8901	17.0213	0.8013	17.3084	0.7305	30.8745	0.8073	21.7347
nnFormer (Zhou et al., 2021a)	0.9094	15.5839	0.8104	15.9412	0.7418	29.4407	0.8205	20.3219
UNETR (Hatamizadeh et al., 2022)	0.9072	15.9829	0.8221	14.9555	0.7632	27.4703	0.8308	19.4696
SwinUNETR (Tang et al., 2022)	0.9182	14.0585	0.8344	11.9582	0.7707	14.6027	<u>0.8411</u>	13.5398
UNesT	0.9262	14.4628	0.8471	8.3677	0.7958	9.735	0.8564*	10.1885

Table 4: Comparison of volumetric analysis metrics between the proposed method and the state-of-the-art clinical study on kidney components.

Metrics	Cortex		Medulla		Pelvicalyceal System	
	(Tang et al., 2021b)	UNesT	(Tang et al., 2021b)	UNesT	(Tang et al., 2021b)	UNesT
R Squared	0.9200	0.9348	0.6652	0.6850	0.4586	0.6126
Pearson R	0.9838	0.9896	0.8156	0.8428	0.6772	0.7454
Absolute Deviation of Volume	3.0233	2.5259	3.5496	3.0293	0.9443	0.7410
Percentage Difference	4.8280	3.8411	7.4750	6.894	19.0716	12.0171

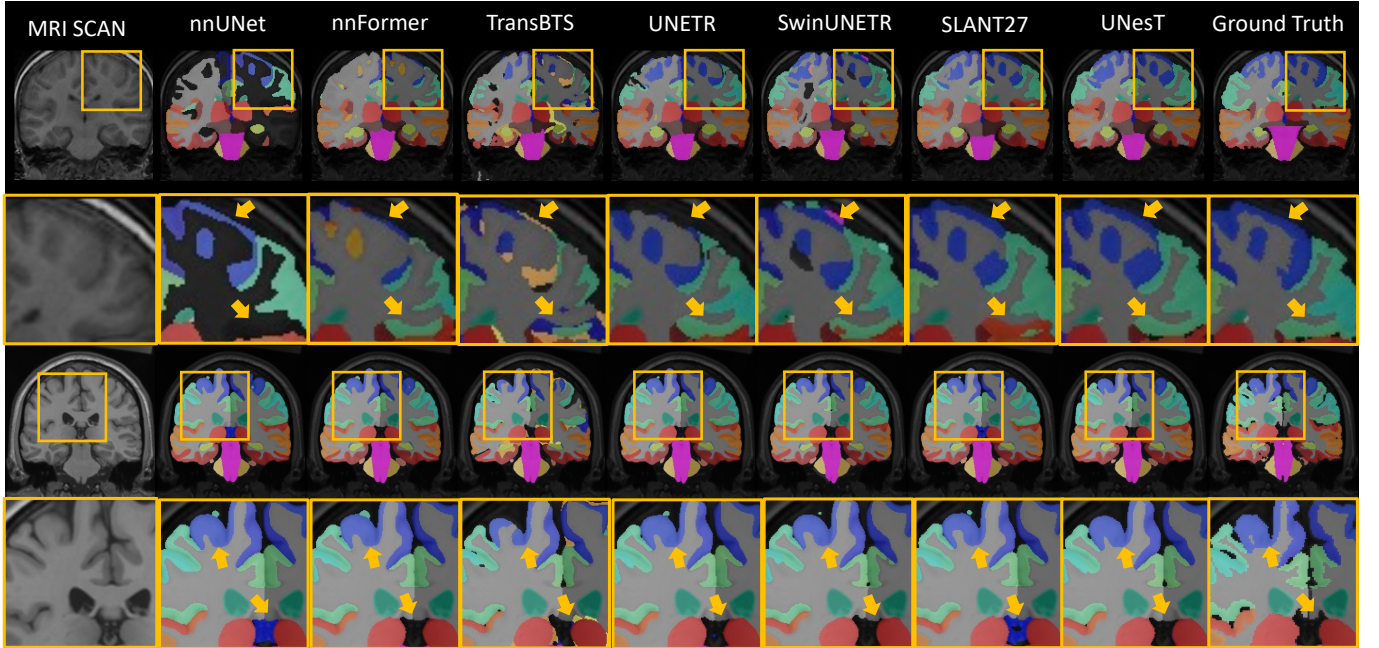


Figure 5: Qualitative results of whole brain segmentation on the CANDI dataset (top 2 rows) and Colin dataset (bottom 2 row). Boxed areas are enlarged in the lower row. Differences are emphasized with the orange arrow. UNesT shows better captures the boundary and correctly segment the tissues.

UNesT-B and UNesT-L) by scaling the depth, heads and width of the transformer. Detailed parameters of UNesT models with various hyperparameter settings are shown in Table 7. Experiments are performed on whole brain segmentation task with 50 T1w MRI scans from OASIS dataset. 45 T1w scans are used for training and the other 5 for validation. No pre-training is performed for all the models. We start with 20% of the training data and added 20% each time until all data are included. All models are trained five times with 9, 18, 27, 36 and 45 samples, respectively. Fig. 10(a) and (b) shows the quantitative results

of DSC in CANDI and Colin dataset, respectively. Fig. 10(c) shows the distribution of the average DSC in each subject of the test set. Fig. 11 shows the qualitative comparison of whole brain segmentation of different model scale trained with 45 T1w scans.

We observe that larger models and additional data improve segmentation performance. Larger models are more data efficient as with the amount of training data increase, larger model perform better than smaller models. In Fig. 11, compared with UNesT-S and UNesT-B, UNesT-S evidently mis-classified a

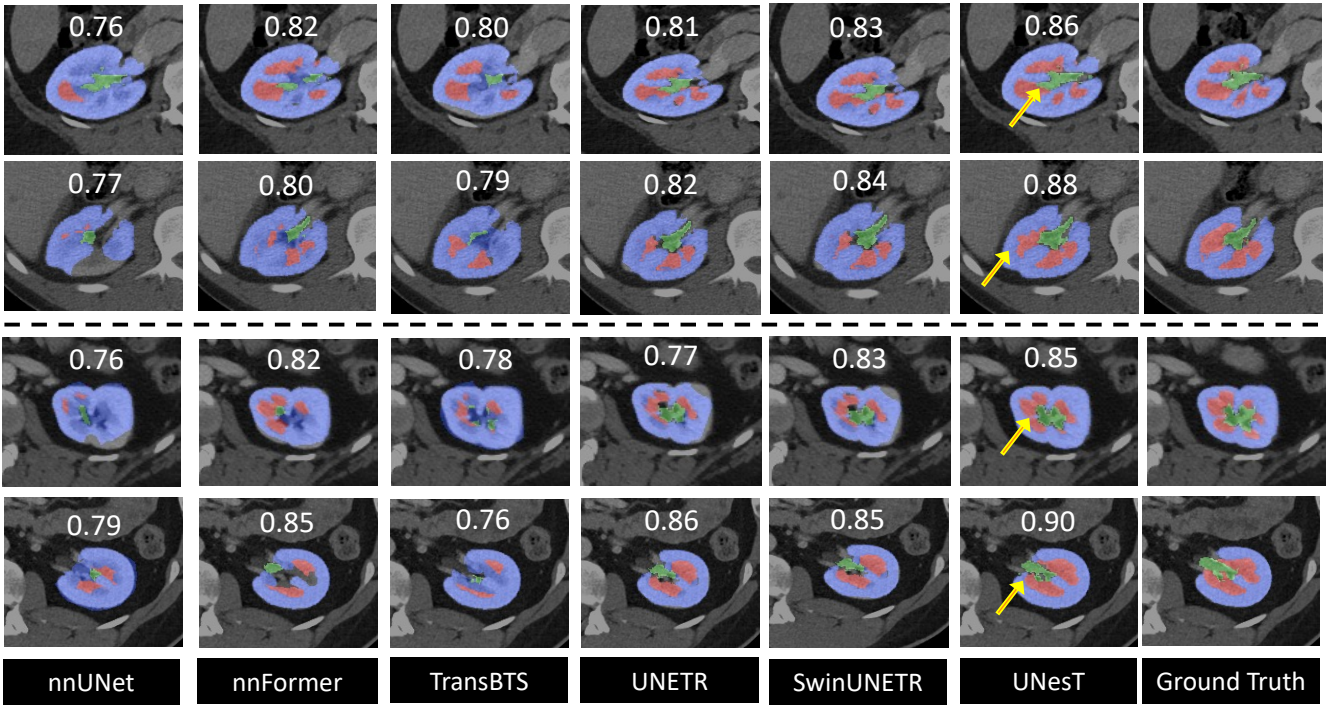


Figure 6: Qualitative comparisons of representative renal sub-structures segmentation on two right (top) and two left (bottom) kidneys. The average DSC is marked on each image. UNesT shows distinct improvement on the medulla (red) and pelvicalyceal system (green) against baselines.

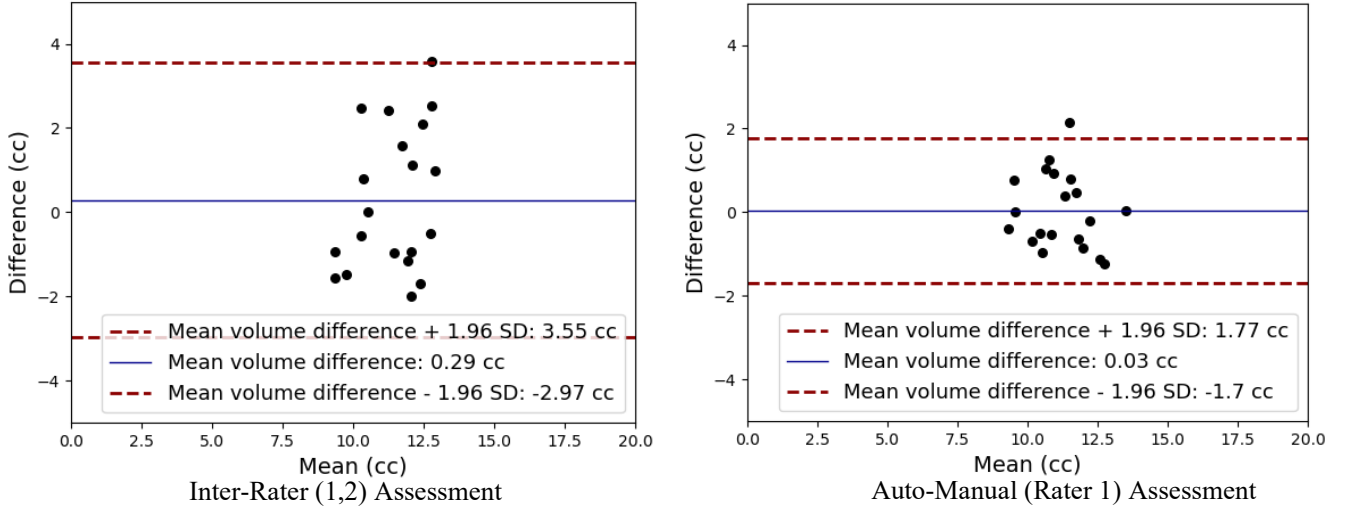


Figure 7: The Bland-Atman plots compare the medulla volume agreement of inter-rater and auto-manual assessment. We show cross-validation on interpreter 1 and interpreter 2 manual segmentation on the same test set. Interpreters present independent observation without communication. The auto-manual assessment shows the agreement between UNesT and interpreter 1 annotations.

large amount of background and brain tissues pixels whereas UNesT-B has mostly clean background indicating that UNesT-B better utilizes the training data efficiently. UNesT-L further improves the segmentation results indicating that larger models are more data efficient. In terms of reducing annotation effort, both UNesT-B and UNesT-L perform better with 9 training samples than UNesT-S with all the training samples, which reduce the annotation effort by at least 80%. When adding additional data, the DSC score increases for all the models of different scales.

In terms of the relationship between model size and DSC score performance, although the DSC score performance steadily increase as the model scale increases, the performance difference become smaller. In low-data regime, UNesT-B can achieve comparable DSC compared to UNesT-L, but UNesT-B marginally outperform UNesT-S. When all the training data are included, the performance increase ratio between UNesT-B and UNesT-S is 5.41% (0.6941 versus 0.6585) compared with 1.83% between UNesT-S and UNesT-B (0.7068 versus 0.6941) on the Colin

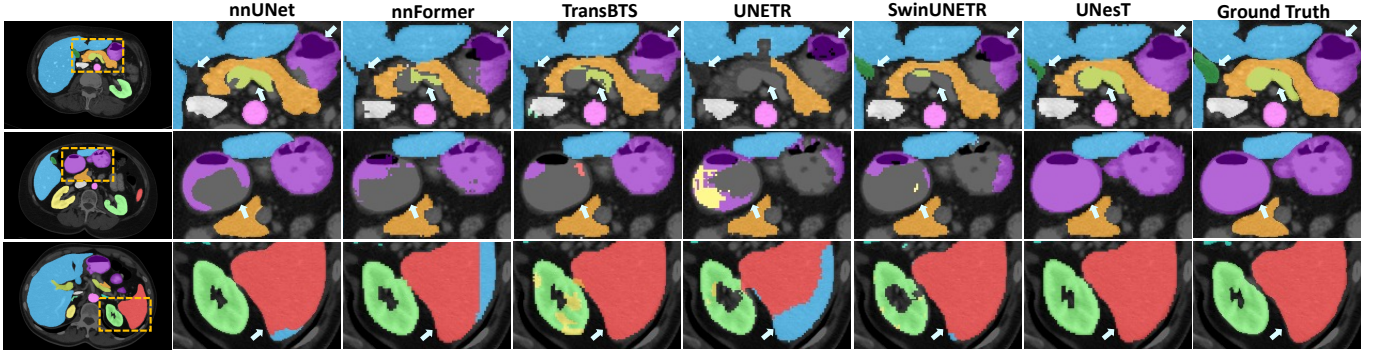


Figure 8: Qualitative comparison between UNesT and baseline methods on the BTCV data. Three representative cases are shown. The region with visual improvement is boxed and enlarged. White arrows emphasized the segmentation improvement on portal vein (yellow), stomach (purple), gallbladder (dark green), left kidney (light green), and spleen (red).

Table 5: Quantitative comparison of the segmentation results on the BTCV testing set. All results shown are single model performance (without ensemble). Our model achieves the overall best performance. Note: RKid: right kidney, LKid: left kidney, Gall: gallbladder, Eso: esophagus, Stom: Stomach, Panc: pancreas, RAG: right adrenal gland, LAG: left adrenal gland.

Methods	Spleen	RKid	LKid	Gall	Eso	Liver	Stom	Aorta	IVC	PSV	Panc	RAG	LAG	Avg
nnUNet	0.9595	0.8835	0.9302	0.7013	0.7672	0.9651	0.8679	0.8893	0.8289	0.7851	0.7960	0.7326	0.6835	0.8316
TransBTS	0.9455	0.8920	0.9097	0.6838	0.7561	0.9644	0.8352	0.8855	0.8248	0.7421	0.7602	0.6723	0.6703	0.8131
nnFormer	0.9458	0.8862	0.9368	0.6529	0.7622	0.9617	0.8359	0.8909	0.8080	0.7597	0.7787	0.7020	0.6605	0.8162
UNETR	0.9048	0.8251	0.8605	0.5823	0.7121	0.9464	0.7206	0.8657	0.7651	0.7037	0.6606	0.6625	0.6304	0.7600
SwinUNETR	0.9459	0.8897	0.9239	0.6537	0.7543	0.9561	0.7557	0.8828	0.8161	0.7630	0.7452	0.6823	0.6602	0.8044
UNesT	0.9580	0.9249	0.9396	0.7002	0.7940	0.9657	0.8861	0.8899	0.8412	0.7856	0.8058	0.7372	0.7083	0.8433

Table 6: KiTS19 DSC performance comparison with baseline methods. The UNesT achieves highest DSC on the with-held test set.

Model	Kidney	Tumor	Avg
nnUNet (Isensee et al., 2021)	0.9643	0.8287	0.8965
nnFormer (Zhou et al., 2021a)	0.9723	0.8348	0.9036
TransBTS (Wang et al., 2021c)	0.9740	0.8374	0.9057
UNETR (Hatamizadeh et al., 2022)	0.9746	0.8382	0.9064
Swin UNETR (Tang et al., 2022)	0.9751	0.8397	0.9074
UNesT (Ours)	0.9794	0.8439	0.9117

Table 7: Model parameters of different scales. Depth: number of transformer layers, Heads: number of heads in the multi-head attention, Width: embedded dimension. Each number in the bracket represent the corresponding hyperparameter in that hierarchy.

Model	#Param	Depth	Heads	Width
UNesT-S	22.4M	(2,2,8)	(2,4,8)	(64,128,256)
UNesT-B	87.3M	(2,2,8)	(4,8,16)	(128,256,512)
UNesT-L	279.6M	(2,2,20)	(6,12,24)	(192,384,768)

dataset and 3.93% (0.6244 versus 0.6008) versus 3.04% (0.6434 versus 0.6244) on the CANDI dataset. Although UNesT-L has 3 times more parameters than UNesT-B, the comparable performance between UNesT-L and UNesT-B indicates UNesT-B is efficient for the training data. After reaching a certain point, scaling up models may not necessarily lead to large performance improvements.

5.5.2. Data Efficiency

We investigate the data efficiency of our proposed method using whole brain and renal substructures dataset. Fig. 11

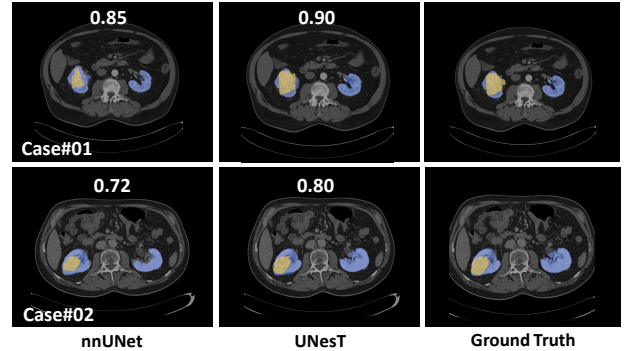


Figure 9: Qualitative comparison between our transformer-based segmentation method and the CNN-based nnUNet model. UNesT shows better tumor segmentation, and we observe the model can better distinguish the kidney-tumor boundary.

show the performance comparison between different UNesT variants, base and larger model are of better data-efficient when training with less data (e.g., 9 or 18). We show the UNesT-B model achieves 133 classes segmentation of DSC 0.6131 with only 9 training samples. Figure 12 shows the data efficiency evaluated and compared on the renal substructure dataset. UNesT achieves DSC of 0.7903 compare to second-best SwinUNETR 0.7681 when training with 20% samples. With the increase of training data, our method performs consistently higher DSC compare to baseline methods. We observe the UNesT model trained with 20% data is comparable to nnUNet or TransBTS using full training data, which show the superior data efficiency.

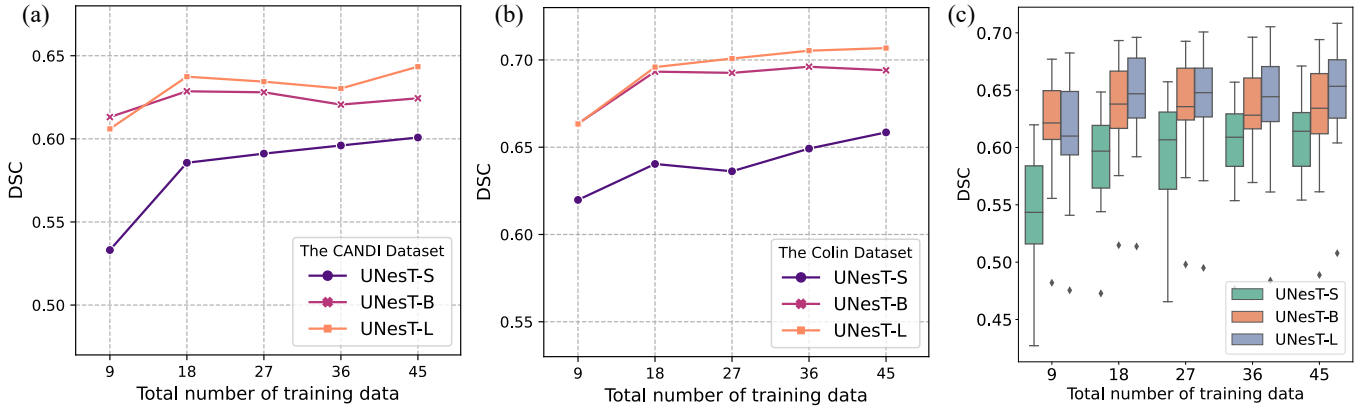


Figure 10: Comparison of segmentation results of models with different scales trained with different percentages of training data. (a) and (b) shows the test results of the Candi and Colin dataset, respectively. (c) shows the results in both the Candi and Colin dataset.

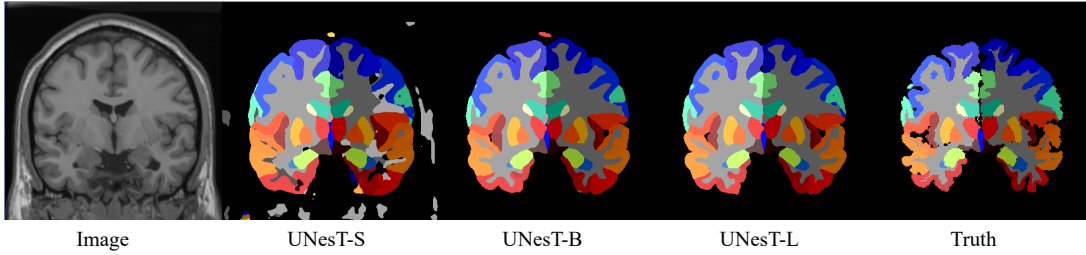


Figure 11: Visualization of segmentation results for each model scale trained with the same number of data. Comparing UNesT-S and UNesT-B, UNesT-S evidently mis-classified a large amount of background and brain tissues pixels whereas UNesT-B has mostly clean background indicating that UNesT-B have better capability on utilizing the training data efficiently. UNesT-L further improves the segmentation results indicating that larger models are more data efficient.

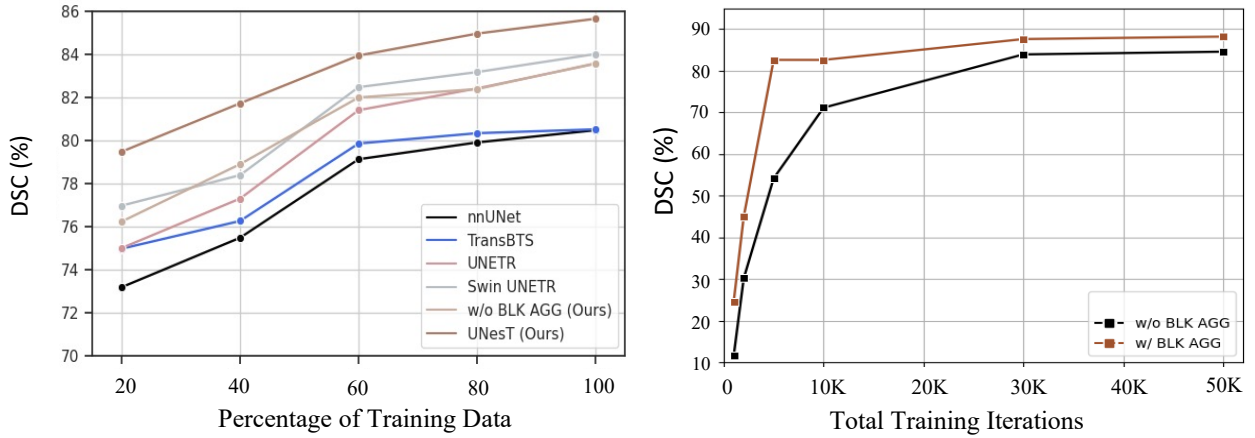


Figure 12: Left: DSC comparison on the test set at different percentages of training samples. Right: Comparison of the convergence rate for the proposed method with and without hierarchical modules, and validation DSC along training iterations are demonstrated.

5.5.3. Effects of Block Aggregation

We show the hierarchical architecture design (with 3D block aggregation) provide significant improvement for medical image segmentation (as shown in Fig. 12). The result shows that the hierarchy mechanism achieves superior performance at 20% to 100% of training data. Under a low-data regime, block aggregation achieves a higher improvement ($> 3\%$ of DSC) compared to

the second-best method. We notice that the model without block aggregation (canonical transformer layers) obtains lower performance. In addition, UNesT with block aggregation demonstrates a faster convergence rate (15% and 4% difference at 2K/30K iterations) compared to the backbone model without hierarchies. The results show block aggregation is an effective component for representation learning for transformer-based models. In ad-

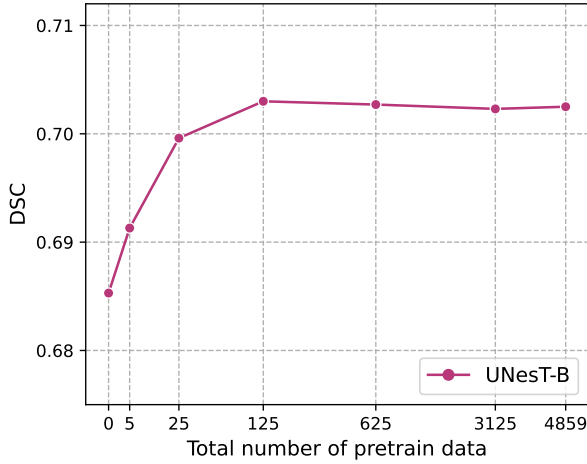


Figure 13: DSC comparison on whole brain segmentation CANDI dataset with different amount of data with pseudo labels for pre-training.

dition, compared with the Swintransformer-based method, our UNesT show consistently superior performance, especially in whole brain segmentation, which indicates the 3D aggregation modules perform better than shifted window module for local patch communication.

5.5.4. Size of pre-training dataset in whole brain segmentation

Acquiring human annotation is labor intensive, thus many studies (Yang et al., 2022; Roy et al., 2017; Huo et al., 2019) adopt the strategy of pre-training with pseudo labels and then finetuning with human annotations to get around this limitation and increase model performance. Herein, we perform experiments of using different amounts of pre-training data in the whole brain segmentation to investigate the impact of pre-training data quantity on the final results. We repeat the experiments 6 times with 5, 25, 125, 625, 3125, and all available pre-training data, respectively. All the pre-trained models are finetuned using the OASIS dataset in the same 5-fold cross-validation setting. We include the results of the training from scratch using the OASIS dataset for comparison. The results are shown in Fig. 13. We observe that increasing the number of pre-trained examples up to 125 resulted in a rapid improvement in DSC score. Pre-training sizes greater than 125 do not further advance performance and the results fluctuate in a small range. This observation demonstrates that UNesT can benefit from pre-training using pseudo data, but a large pre-training dataset is not a necessity. When the amount of pre-training data reaches a certain limit, the performance gains are reduced. Instead, adding more pseudo data could possibly confuse the network.

6. Discussion

6.1. Why we need an efficient hierarchical transformer-based medical segmentation model?

In this paper, we target the critical problem that transformed-based models commonly lack of local positional information

resulting in sub-optimal performance when handling considerable tissue classes in 3D medical image segmentation. Specifically, medical segmentation datasets are small where images are of spatially high-resolution and high dimensionality which can lead to data inefficiency. Our proposed UNesT address the above problem by aggregating the spatially adjacent patches in a hierarchical way and leveraging the global self-attention mechanism to combine global and local information efficiently. SwinUNETR (Tang et al., 2022), which uses "shifted window" for local patch communication, observed good but inconsistent performance. Specifically, it achieves second-best performance in the renal substructures segmentation but in the whole brain segmentation, its DSC scores in test datasets under-perform the second-best performing SLANT27 model by a large margin. Our method consistently achieves superior results on the four evaluated heterogeneous tasks.

We highlight the success of segmentation with a single UNesT model compared to the prior state-of-the-art method SLANT27 (Huo et al., 2019), which used 27 ensemble networks. Among current 3D medical image segmentation methods, we address the challenging tasks, including more than one hundred structures in T1w MRI, three inter-connected components in kidneys, thirteen major organs in the abdomen, and kidney-tumor connected tissue.

The superior performance of UNesT in these inferences 4 different tasks demonstrates the effectiveness and efficiency of UNesT in segmenting multiple structures/tissues with small medical datasets. Specifically, we validate that our model is data efficient in low-data regimes. Moreover, our experiments show that larger models are more data efficient, suggesting the proposed network is easily scalable if necessary. Furthermore, we study the impact of the number of pseudo labels used for pre-training. We observed that pre-training sizes exceeding a certain number do not further advance model performance. On the contrary, adding more pseudo labels may confuse the network and decrease performance (Fig. 13).

6.2. Reproducibility against clinical radiologists

In this work, we develop the first in-house renal sub-structures CT cohort for segmentation including the renal cortex, medulla, and pelvicalyceal system which are manually annotated by radiologists. We show that the proposed method is data-efficient for accurately quantifying kidney components and can be used for volumetric analysis such as in the medullary pyramids. Figure 7 shows the proposed automatic segmentation method achieves better agreement compared to inter-rater assessment, with 0.03 versus 0.29 mean difference, respectively, indicating robust reproducibility. Visual quantitative analysis of renal structures remains a complex task for radiologists. Some of the histomorphometric features in regions of the kidney (e.g., textural or graph features) are poorly adapted for manual identification. In this study, we show that UNesT achieves consistently reliable performance. Compared with previous studies on cortex segmentation, the proposed approach significantly facilitates the derivation of the visual and quantitative results.

6.3. Limitation and sensitivity study

For whole brain segmentation, we observe current performance is limited by registration. Specifically, the DSC score in MNI space is around 0.90 and around 0.87 in the Colin and CANDI dataset, respectively. However, the performance drops around 0.17 DSC score after inverse transformation to the original space. Investigation of registration performance should be considered in the future.

We study outlier cases of renal structure segmentation to demonstrate potential limitations. In reviewing most computer-automated segmentation methods, we found about 90% of the segmentation is promising, but about 10% are also found to be outliers. As shown in Fig. 14, typical outliers under-segment and fail to capture parts of tissue labels (left two images). The missing parts result in a lower DSC score of about 0.80 (cortex) and 0.62 (medulla). The right two images show the other type of failure: over-segmentation, where we observe a complete renal segmentation but mis-labeling of nearby tissues. This issue can potentially be resolved by component analysis in a post-processing step. These two types of outlier segmentation are easily spotted with a rudimentary visual quality check.

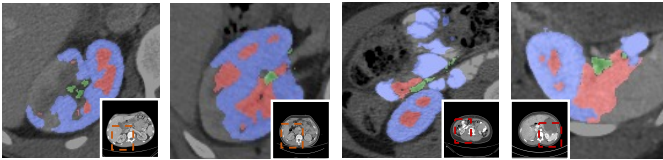


Figure 14: Demonstration of potential outlier cases. The left two images show representative under-labeling of tissues. The right two images show the over-labeling of tissues. These segmentations are computed on additional contrast-enhanced CT scans without ground truth labels.

7. Conclusions

In this paper, we propose a novel hierarchical transformer-based 3D medical image segmentation approach (UNesT) with a 3D block aggregation module to achieve local communication. We validate the effectiveness of UNesT on 4 different tasks in both CT and MRI modalities including a whole brain segmentation task with 133 classes, a renal substructure segmentation task, a multi-organ abdominal segmentation task, and a kidney/tumor segmentation task. We consistently achieve state-of-the-art performance on the four datasets. Our single model outperforms 27 ensemble models in the prior state-of-the-art method, SLANT27, for whole brain segmentation. In addition, we develop the first in-house renal sub-structures CT dataset with radiologists. UNesT achieves the best performance among recent popular convolutional- and transformer-based volumetric medical segmentation methods. We show the major contribution of the proposed method on successfully modeling hundreds of tissues (e.g., 133 classes) and hierarchically inter-connected structures.

Acknowledgments

This research is supported by NIH Common Fund and National Institute of Diabetes, Digestive and Kidney Diseases U54DK120058, NSF CAREER 1452485, NIH grants, 2R01EB006136, 1R01EB017230 (Landman), and R01NS09529. The identified datasets used for the analysis described were obtained from the Research Derivative (RD), database of clinical and related data. The imaging dataset(s) used for the analysis described were obtained from ImageVU, a research repository of medical imaging data and image-related metadata. ImageVU and RD are supported by the VICTR CTSA award (ULTR000445 from NCATS/NIH) and Vanderbilt University Medical Center institutional funding. ImageVU pilot work was also funded by PCORI (contract CDRN-1306-04869).

References

- Asman, A.J., Landman, B.A., 2014. Hierarchical performance estimation in the statistical label fusion framework. *Medical image analysis* 18, 1070–1081.
- Aubert-Broche, B., Evans, A.C., Collins, L., 2006. A new improved version of the realistic digital brain phantom. *NeuroImage* 32, 138–145.
- Beltagy, I., Peters, M.E., Cohan, A., 2020. Longformer: The long-document transformer. *arXiv preprint arXiv:2004.05150*.
- Ç., Ö., Abdulkadir, A., Lienkamp, S.S., Brox, T., Ronneberger, O., 2016. 3d u-net: learning dense volumetric segmentation from sparse annotation, in: *MICCAI*, Springer.
- Cao, H., Wang, Y., Chen, J., Jiang, D., Zhang, X., Tian, Q., Wang, M., 2021. Swin-unet: Unet-like pure transformer for medical image segmentation. *arXiv preprint arXiv:2105.05537*.
- Chang, Y., Menghan, H., Guangtao, Z., Xiao-Ping, Z., 2021. Transclaw u-net: Claw u-net with transformers for medical image segmentation. *arXiv preprint arXiv:2107.05188*.
- Chen, B., Liu, Y., Zhang, Z., Lu, G., Zhang, D., 2021a. Transattunet: Multi-level attention-guided u-net with transformer for medical image segmentation. *arXiv preprint arXiv:2107.05274*.
- Chen, J., Lu, Y., Yu, Q., Luo, X., Adeli, E., Wang, Y., Lu, L., Yuille, A.L., Zhou, Y., 2021b. Transunet: Transformers make strong encoders for medical image segmentation. *arXiv preprint arXiv:2102.04306*.
- Chen, X., Summers, R.M., Cho, M., Bagci, U., Yao, J., 2012. An automatic method for renal cortex segmentation on ct images: evaluation on kidney donors. *Academic radiology*.
- Cordonnier, J.B., Loukas, A., Jaggi, M., 2019. On the relationship between self-attention and convolutional layers. *arXiv preprint arXiv:1911.03584*.

- Deng, K., Meng, Y., Gao, D., Bridge, J., Shen, Y., Lip, G., Zhao, Y., Zheng, Y., 2021. Transbridge: A lightweight transformer for left ventricle segmentation in echocardiography, in: International Workshop on Advances in Simplifying Medical Ultrasound, Springer. pp. 63–72.
- Dong, B., Wang, W., Fan, D.P., Li, J., Fu, H., Shao, L., 2021. Polyp-pvt: Polyp segmentation with pyramid vision transformers. *arXiv preprint arXiv:2108.06932*.
- Dosovitskiy, A., Beyer, L., Kolesnikov, A., Weissenborn, D., Zhai, X., Unterthiner, T., Dehghani, M., Minderer, M., Heigold, G., Gelly, S., et al., 2020. An image is worth 16x16 words: Transformers for image recognition at scale, in: International Conference on Learning Representations.
- Evans, A.C., Collins, D.L., Mills, S., Brown, E.D., Kelly, R.L., Peters, T.M., 1993. 3d statistical neuroanatomical models from 305 mri volumes, in: 1993 IEEE conference record nuclear science symposium and medical imaging conference, IEEE.
- Han, K., Xiao, A., Wu, E., Guo, J., Xu, C., Wang, Y., 2021. Transformer in transformer. *Advances in Neural Information Processing Systems* 34.
- Hatamizadeh, A., Tang, Y., Nath, V., Yang, D., Myronenko, A., Landman, B., Roth, H.R., Xu, D., 2022. Unetr: Transformers for 3d medical image segmentation, in: Proceedings of the IEEE/CVF Winter Conference on Applications of Computer Vision, pp. 574–584.
- Heller, N., Isensee, F., Maier-Hein, K.H., Hou, X., Xie, C., Li, F., Nan, Y., Mu, G., Lin, Z., Han, M., et al., 2021. The state of the art in kidney and kidney tumor segmentation in contrast-enhanced ct imaging: Results of the kits19 challenge. *Medical image analysis* 67, 101821.
- Hu, H., Zhang, Z., Xie, Z., Lin, S., 2019. Local relation networks for image recognition, in: Proceedings of the IEEE/CVF International Conference on Computer Vision, pp. 3464–3473.
- Huang, X., Deng, Z., Li, D., Yuan, X., 2021. Missformer: An effective medical image segmentation transformer. *arXiv preprint arXiv:2109.07162*.
- Huo, Y., Xu, Z., Xiong, Y., A., K., Parvathaneni, P., Bao, S., Bermudez, C., Resnick, S.M., Cutting, L.E., Landman, B.A., 2019. 3d whole brain segmentation using spatially localized atlas network tiles. *NeuroImage*.
- Isensee, F., Jaeger, P.F., Kohl, S.A., Petersen, J., Maier-Hein, K.H., 2021. nnu-net: a self-configuring method for deep learning-based biomedical image segmentation. *Nature Methods* 18, 203–211.
- Jin, C., Shi, F., Xiang, D., Jiang, X., Zhang, B., Wang, X., Zhu, W., Gao, E., Chen, X., 2016. 3d fast automatic segmentation of kidney based on modified aam and random forest. *IEEE transactions on medical imaging* 35, 1395–1407.
- Kennedy, D.N., Haselgrove, C., Hodge, S.M., Rane, P.S., Makris, N., Frazier, J.A., 2012. Candishare: a resource for pediatric neuroimaging data.
- Klein, A., Dal Canton, T., Ghosh, S.S., Landman, B., Lee, J., Worth, A., 2010. Open labels: online feedback for a public resource of manually labeled brain images, in: 16th Annual Meeting for the Organization of Human Brain Mapping.
- Landman, B., Xu, Z., Igelsias, J., Styner, M., Langerak, T., Klein, A., 2015. Miccai multi-atlas labeling beyond the cranial vault—workshop and challenge, in: Proc. MICCAI Multi-Atlas Labeling Beyond Cranial Vault—Workshop Challenge.
- Li, S., Sui, X., Luo, X., Xu, X., Liu, Y., Goh, R., 2021a. Medical image segmentation using squeeze-and-expansion transformers. *arXiv preprint arXiv:2105.09511*.
- Li, Y., Wang, S., Wang, J., Zeng, G., Liu, W., Zhang, Q., Jin, Q., Wang, Y., 2021b. Gt u-net: A u-net like group transformer network for tooth root segmentation, in: International Workshop on Machine Learning in Medical Imaging, Springer. pp. 386–395.
- Li, Y., Wang, Z., Yin, L., Zhu, Z., Qi, G., Liu, Y., 2021c. X-net: a dual encoding–decoding method in medical image segmentation. *The Visual Computer*, 1–11.
- Lin, A., Chen, B., Xu, J., Zhang, Z., Lu, G., 2021. Ds-transunet: Dual swin transformer u-net for medical image segmentation. *arXiv preprint arXiv:2106.06716*.
- Liu, Z., Lin, Y., Cao, Y., Hu, H., Wei, Y., Zhang, Z., Lin, S., Guo, B., 2021. Swin transformer: Hierarchical vision transformer using shifted windows. *Proceedings of the IEEE/CVF International Conference on Computer Vision*.
- Marcus, D.S., Wang, T.H., Parker, J., Csernansky, J.G., Morris, J.C., Buckner, R.L., 2007. Open access series of imaging studies (oasis): cross-sectional mri data in young, middle aged, nondemented, and demented older adults. *Journal of cognitive neuroscience*.
- Meng, X., Zhang, X., Wang, G., Zhang, Y., Shi, X., Dai, H., Wang, Z., Wang, X., 2021. Exploiting full resolution feature context for liver tumor and vessel segmentation via fusion encoder: Application to liver tumor and vessel 3d reconstruction. *arXiv preprint arXiv:2111.13299*.
- Ourselin, S., Roche, A., Subsol, G., Pennec, X., Ayache, N., 2001. Reconstructing a 3d structure from serial histological sections. *Image and vision computing* 19, 25–31.
- Peiris, H., Hayat, M., Chen, Z., Egan, G., Harandi, M., 2021. A volumetric transformer for accurate 3d tumor segmentation. *arXiv preprint arXiv:2111.13300*.
- Ronneberger, O., Fischer, P., Brox, T., 2015. U-net: Convolutional networks for biomedical image segmentation, in: International Conference on Medical image computing and computer-assisted intervention, Springer. pp. 234–241.

- Roth, H.R., Shen, C., Oda, H., Sugino, T., Oda, M., Hayashi, Y., Misawa, K., Mori, K., 2018. A multi-scale pyramid of 3d fully convolutional networks for abdominal multi-organ segmentation, in: International conference on medical image computing and computer-assisted intervention.
- Roy, A.G., Conjeti, S., Sheet, D., Katouzian, A., Navab, N., Wachinger, C., 2017. Error corrective boosting for learning fully convolutional networks with limited data, in: International Conference on Medical Image Computing and Computer-Assisted Intervention, Springer. pp. 231–239.
- Tang, Y., Gao, R., Lee, H.H., Han, S., Chen, Y., Gao, D., Nath, V., Bermudez, C., Savona, M.R., Abramson, R.G., et al., 2021a. High-resolution 3d abdominal segmentation with random patch network fusion. *Medical Image Analysis* 69, 101894.
- Tang, Y., Gao, R., Lee, H.H., Xu, Z., Savoie, B.V., Bao, S., Huo, Y., Fogo, A.B., Harris, R., de Caestecker, M.P., et al., 2021b. Renal cortex, medulla and pelvicaliceal system segmentation on arterial phase ct images with random patch-based networks, in: Medical Imaging 2021: Image Processing, International Society for Optics and Photonics. p. 115961D.
- Tang, Y., Yang, D., Li, W., Roth, H.R., Landman, B., Xu, D., Nath, V., Hatamizadeh, A., 2022. Self-supervised pre-training of swin transformers for 3d medical image analysis, in: Proceedings of the IEEE/CVF Conference on Computer Vision and Pattern Recognition, pp. 20730–20740.
- Tustison, N.J., Avants, B.B., Cook, P.A., Zheng, Y., Egan, A., Yushkevich, P.A., Gee, J.C., 2010. N4itk: improved n3 bias correction. *IEEE transactions on medical imaging* 29, 1310–1320.
- Ulyanov, D., Vedaldi, A., Lempitsky, V., 2016. Instance normalization: The missing ingredient for fast stylization. *arXiv preprint arXiv:1607.08022*.
- Valanarasu, J.M.J., Oza, P., Hacihaliloglu, I., Patel, V.M., 2021. Medical transformer: Gated axial-attention for medical image segmentation. *arXiv preprint arXiv:2102.10662*.
- Wang, B., Dong, P., et al., 2022. Multiscale transunet++: dense hybrid u-net with transformer for medical image segmentation. *Signal, Image and Video Processing*, 1–8.
- Wang, H., Xie, S., Lin, L., Iwamoto, Y., Han, X.H., Chen, Y.W., Tong, R., 2021a. Mixed transformer u-net for medical image segmentation. *arXiv preprint arXiv:2111.04734*.
- Wang, J., Wei, L., Wang, L., Zhou, Q., Zhu, L., Qin, J., 2021b. Boundary-aware transformers for skin lesion segmentation, in: International Conference on Medical Image Computing and Computer-Assisted Intervention, Springer. pp. 206–216.
- Wang, W., Chen, C., Ding, M., Li, J., Yu, H., Zha, S., 2021c. Transbts: Multimodal brain tumor segmentation using transformer. *arXiv preprint arXiv:2103.04430*.
- Wasserthal, J., Meyer, M., Breit, H.C., Cyriac, J., Yang, S., Segeroth, M., 2022. Totalsegmentator: robust segmentation of 104 anatomical structures in ct images. *arXiv preprint arXiv:2208.05868*.
- Wu, Y., Liao, K., Chen, J., Chen, D.Z., Wang, J., Gao, H., Wu, J., 2022. D-former: A u-shaped dilated transformer for 3d medical image segmentation. *arXiv preprint arXiv:2201.00462*.
- Xiang, D., Bagci, U., Jin, C., Shi, F., Zhu, W., Yao, J., Sonka, M., Chen, X., 2017. Cortexpert: A model-based method for automatic renal cortex segmentation. *Medical image analysis* 42, 257–273.
- Xie, Y., Zhang, J., Shen, C., Xia, Y., 2021a. Cotr: Efficiently bridging cnn and transformer for 3d medical image segmentation. *International conference on medical image computing and computer-assisted intervention*.
- Xie, Y., Zhang, J., Xia, Y., Wu, Q., 2021b. Unified 2d and 3d pre-training for medical image classification and segmentation. *arXiv preprint arXiv:2112.09356*.
- Xie, Z., Lin, Y., Yao, Z., Zhang, Z., Dai, Q., Cao, Y., Hu, H., 2021c. Self-supervised learning with swin transformers. *arXiv preprint arXiv:2105.04553*.
- Yan, X., Tang, H., Sun, S., Ma, H., Kong, D., Xie, X., 2022. After-unet: Axial fusion transformer unet for medical image segmentation, in: Proceedings of the IEEE/CVF Winter Conference on Applications of Computer Vision, pp. 3971–3981.
- Yang, Q., Yu, X., Lee, H.H., Tang, Y., Bao, S., Gravenstein, K.S., Moore, A.Z., Makrogiannis, S., Ferrucci, L., Landman, B.A., 2022. Label efficient segmentation of single slice thigh ct with two-stage pseudo labels. *Journal of Medical Imaging* 9, 052405.
- Zhai, X., Kolesnikov, A., Houlsby, N., Beyer, L., 2021. Scaling vision transformers. *arXiv preprint arXiv:2106.04560*.
- Zhang, Y., Liu, H., Hu, Q., 2021a. Transfuse: Fusing transformers and cnns for medical image segmentation. *arXiv preprint arXiv:2102.08005*.
- Zhang, Z., Sun, B., Zhang, W., 2021b. Pyramid medical transformer for medical image segmentation. *arXiv preprint arXiv:2104.14702*.
- Zhang, Z., Zhang, H., Zhao, L., Chen, T., Arik, S.O., Pfister, T., 2021c. Nested hierarchical transformer: Towards accurate, data-efficient and interpretable visual understanding. *arXiv preprint arXiv:2105.12723*.
- Zhou, H.Y., Guo, J., Zhang, Y., Yu, L., Wang, L., Yu, Y., 2021a. nnformer: Interleaved transformer for volumetric segmentation. *arXiv preprint arXiv:2109.03201*.
- Zhou, Z., Siddiquee, M.M.R., Tajbakhsh, N., Liang, J., 2018. Unet++: A nested u-net architecture for medical image segmentation, in: Deep learning in medical image analysis and multimodal learning for clinical decision support. Springer, pp. 3–11.

- Zhou, Z., Sodha, V., Pang, J., Gotway, M.B., Liang, J., 2021b. Models genesis. *Medical image analysis* 67, 101840.
- Zhu, Z., Xia, Y., Shen, W., Fishman, E., Yuille, A., 2018. A 3d coarse-to-fine framework for volumetric medical image segmentation, in: 2018 International conference on 3D vision (3DV), IEEE. pp. 682–690.

Appendix

This work is the first effort to evaluate comprehensive benchmarks for whole brain segmentation and renal substructure segmentation for 3D medical image analysis. We extend the most representative and challenging whole brain segmentation task’s performance, and show complete performance table for all 133 structures in Appendix A. In section B, we introduce the open-source project availability development based on UNesT and the study.

A. Whole Brain Segmentation Details

A.1. Data Pre-processing

We apply N4 bias field correction (Tustison et al., 2010) on the images after registration. We use robust regression (robustfit) in Matlab to normalize the MRI scans in the test set. To train the regression model, inputs are normalized by: $I' = \frac{I - \mu}{\sigma}$, where I is the original image, I' is the normalized output image, μ is the image mean, and σ is the image standard deviation. I' is then masked by a binary map where the brain tissues label probability larger than 0.5 is 1 otherwise 0 to get I_{mask} . The sorted I_{mask} is averaged by all the images in the training set to train the regression model. During the testing, the weights are learned gradually. The learned weights are used to normalized test scans. Please refer to (Huo et al., 2019) for more details.

A.2. Detailed Brain Regions and Performance

A detailed brain regions included in the whole brain segmentation task is shown in Table A.8, in which 30, 31, and 32 are not presented in both the Colin and the CANDI dataset and thus excluded for evaluation. Quantitative performance comparison of 130 classes is shown in Fig. A.17.

B. Open-Source Availability

For developing public available segmentation tools. We introduce the MONAI Bundle module that supports building Python-based workflows via structured configurations. The authors contribute and develop the bundle code that benefits in four fold:

- Run as normal Python command, integrated into MONAI package, no additional installations.
- Compare to Docker container, Bundle configuration provides good readability and usability by separating system parameter settings from the Python code.
- The pipeline demonstrate workflow at a higher level and allows for changes and customized implementations.
- Support labeling with visualization tool plugins such as 3D Slicer.

The tutorial and release of code/model for whole brain segmentation using the 3D transformer-based segmentation model UNesT is released at:

wholeBrainSeg-Large-UNesT-segmentation.

The renal substructure tutorial is released at:

renalStructures-UNesT-segmentation

B.1. Run with python command

Follow and set path for environments and run command:

```
python -m monai.bundle run evaluating
--meta_file configs/metadata.json
--config_file configs/inference.json
--loggings_file configs/logging.conf
```

B.2. Run with 3D Slicer and MONAI Label

We developed a server-based tool for integrating annotation whole brain and renal substructures purpose as shown in Figure. B.15 and B.16. Install MONAI Label to work on labeling with public visualization tools such as 3D Slicer, renal structures segmentation as the Tutorial. Run command to start server with renal or whole brain segmentation with UNesT model:

```
# start the bundle app in MONAI label

monailabel start_server --app <full path
to the monaibundle app/monaibundle>
--studies <path to the local dataset>
--conf models
renalStructures_UNesT_segmentation_v0.1.0
```

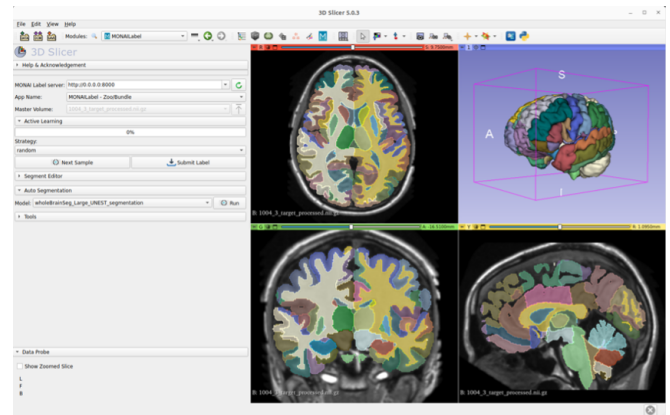


Figure B.15: Server-based whole brain segmentation using large UNesT annotation model and inference with 3D Slicer.

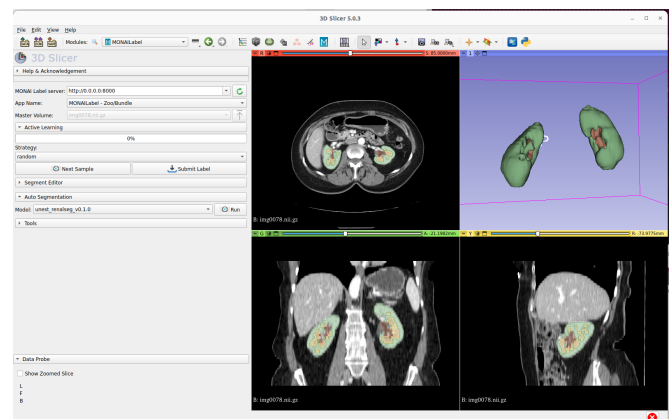


Figure B.16: Server-based renal substructure segmentation using base UNesT annotation model and inference with 3D Slicer



Figure A.17: Quantitative results of 130 classes in the whole brain segmentation task. Scatters show the mean DSC score of each methods. Overall UNesT have the most best performing classes.

Table A.8: List of classes in the whole brain segmentation task. Note: "*" represent the 3 classes not included in the Colin and CANDI dataset.

0	Background	67	Right MCgG middle cingulate gyrus
1	3rd Ventricle	68	Left MCgG middle cingulate gyrus
2	4th Ventricle	69	Right MFC medial frontal cortex
3	Right Accumbens Area	70	Left MFC medial frontal cortex
4	Left Accumbens Area	71	Right MFG middle frontal gyrus
5	Right Amygdala	72	Left MFG middle frontal gyrus
6	Left Amygdala	73	Right MOG middle occipital gyrus
7	Brain Stem	74	Left MOG middle occipital gyrus
8	Right Caudate	75	Right MORG medial orbital gyrus
9	Left Caudate	76	Left MORG medial orbital gyrus
10	Right Cerebellum Exterior	77	Right MPoG postcentral gyrus medial segment
11	Left Cerebellum Exterior	78	Left MPoG postcentral gyrus medial segment
12	Right Cerebellum White Matter	79	Right MPrG precentral gyrus medial segment
13	Left Cerebellum White Matter	80	Left MPrG precentral gyrus medial segment
14	Right Cerebral White Matter	81	Right MSFG superior frontal gyrus medial segment
15	Left Cerebral White Matter	82	Left MSFG superior frontal gyrus medial segment
16	Right Hippocampus	83	Right MTG middle temporal gyrus
17	Left Hippocampus	84	Left MTG middle temporal gyrus
18	Right Inf Lat Vent	85	Right OCP occipital pole
19	Left Inf Lat Vent	86	Left OCP occipital pole
20	Right Lateral Ventricle	87	Right OFuG occipital fusiform gyrus
21	Left Lateral Ventricle	88	Left OFuG occipital fusiform gyrus
22	Right Pallidum	89	Right OpIFG opercular part of the inferior frontal gyrus
23	Left Pallidum	90	Left OpIFG opercular part of the inferior frontal gyrus
24	Right Putamen	91	Right OrIFG orbital part of the inferior frontal gyrus
25	Left Putamen	92	Left OrIFG orbital part of the inferior frontal gyrus
26	Right Thalamus Proper	93	Right PCgG posterior cingulate gyrus
27	Left Thalamus Proper	94	Left PCgG posterior cingulate gyrus
28	Right Ventral DC	95	Right PCu precuneus
29	Left Ventral DC	96	Left PCu precuneus
30*	Cerebellar Vermal Lobules I-V	97	Right PHG parahippocampal gyrus
31*	Cerebellar Vermal Lobules VI-VII	98	Left PHG parahippocampal gyrus
32*	Cerebellar Vermal Lobules VIII-X	99	Right Plns posterior insula
33	Left Basal Forebrain	100	Left Plns posterior insula
34	Right Basal Forebrain	101	Right PO parietal operculum
35	Right ACgG anterior cingulate gyrus	102	Left PO parietal operculum
36	Left ACgG anterior cingulate gyrus	103	Right PoG postcentral gyrus
37	Right AIns anterior insula	104	Left PoG postcentral gyrus
38	Left AIns anterior insula	105	Right POrG posterior orbital gyrus
39	Right AORg anterior orbital gyrus	106	Left POrG posterior orbital gyrus
40	Left AORg anterior orbital gyrus	107	Right PP planum polare
41	Right AnG angular gyrus	108	Left PP planum polare
42	Left AnG angular gyrus	109	Right PrG precentral gyrus
43	Right Calc calcarine cortex	110	Left PrG precentral gyrus
44	Left Calc calcarine cortex	111	Right PT planum temporale
45	Right CO central operculum	112	Left PT planum temporale
46	Left CO central operculum	113	Right SCA subcallosal area
47	Right Cun cuneus	114	Left SCA subcallosal area
48	Left Cun cuneus	115	Right SFG superior frontal gyrus
49	Right Ent entorhinal area	116	Left SFG superior frontal gyrus
50	Left Ent entorhinal area	117	Right SMC supplementary motor cortex
51	Right FO frontal operculum	118	Left SMC supplementary motor cortex
52	Left FO frontal operculum	119	Right SMG supramarginal gyrus
53	Right FRP frontal pole	120	Left SMG supramarginal gyrus
54	Left FRP frontal pole	121	Right SOG superior occipital gyrus
55	Right FuG fusiform gyrus	122	Left SOG superior occipital gyrus
56	Left FuG fusiform gyrus	123	Right SPL superior parietal lobule
57	Right GRe gyrus rectus	124	Left SPL superior parietal lobule
58	Left GRe gyrus rectus	125	Right STG superior temporal gyrus
59	Right IOG inferior occipital gyrus	126	Left STG superior temporal gyrus
60	Left IOG inferior occipital gyrus	127	Right TMP temporal pole
61	Right ITG inferior temporal gyrus	128	Left TMP temporal pole
62	Left ITG inferior temporal gyrus	129	Right TrIFG triangular part of the inferior frontal gyrus
63	Right LiG lingual gyrus	130	Left TrIFG triangular part of the inferior frontal gyrus
64	Left LiG lingual gyrus	131	Right TTG transverse temporal gyrus
65	Right LORg lateral orbital gyrus	132	Left TTG transverse temporal gyrus
66	Left LORg lateral orbital gyrus		